H^- formation in collisions of hydrogen atoms with an Al(100) surface

Boyan Obreshkov

James R. Macdonald Laboratory, Department of Physics, Kansas State University, Manhattan, Kansas 66506, USA and Institute for Nuclear Research and Nuclear Energy, Bulgarian Academy of Sciences, Tsarigradsko Chaussée 72, Sofia 1784, Bulgaria

Uwe Thumm

James R. Macdonald Laboratory, Department of Physics, Kansas State University, Manhattan, Kansas 66506, USA

(Received 16 January 2013; published 22 February 2013)

We theoretically investigate the electron transfer dynamics during the reflection of hydrogen atoms on an Al(100) surface for a wide range of collision energies below 6 keV. We find a nonmonotonic variation of the hydrogen-negative-ion fractions as functions of the projectile impact velocity due to nonadiabatic electron transfer. Our calculated anion fractions for projectiles scattered along high Miller-index crystal-surface directions are in good quantitative agreement with measured H^- fractions for a wide range of exit velocities.

DOI: 10.1103/PhysRevA.87.022903 PACS number(s): 79.20.Rf

I. INTRODUCTION

The analysis of measured final charge states of surface-reflected projectiles yields quantitative information about the electron-transfer dynamics. Theoretical schemes for modeling charge exchange in ion-surface collisions can reveal deviations from the adiabatic evolution of the initial charge state of the projectile and provide reliable estimates for the fractions of minority charge states of the atom after its reflection from the surface. A number of such scattering experiments has been performed in the past, allowing for the scrutiny of various theoretical models [1–3].

An essential determinant of the final projectile charge state is the projectile impact velocity **v**. Theoretical investigations [4,5] showed that resonant charge transfer at surfaces is strongly affected by the characteristics of the surface electronic band structure and by the surface-specific interaction time and projectile charge-state evolution along the surface-reflected trajectory. For the particular case of H^- interacting with Cu(111) metal surfaces, which support an L-band gap, it was demonstrated that for long ion-surface interaction times the active electron has enough time to respond sensitively to details of the substrate electronic structure and that the electronic dynamics of the collision system evolves adiabatically, consistent with the fixed-ion approximation [6–8]. In contrast, for short interaction times, details of the substrate electronic structure are not resolved, and the time evolution of the collision system is well described by a structureless jellium model for the target electronic distribution [9]. This prediction has been confirmed experimentally [10] by measuring hydrogen and fluorine negative-ion fractions on L-band-gap Ag(111) surfaces as functions of the projectile exit-velocity component in the direction perpendicular to the surface.

The calculated hydrogen negative-ion fractions on Ag(111) and Ag(100) surfaces of Ref. [11] are in good agreement with the experimental result of Ref. [10] for larger exit angles to the surface and large interaction times. By comparing the ion fractions for two different orientations of the Ag surfaces [(100) and (111)], a critical dependence on the three Miller indices was observed, indicating that electron transfer near the surface can depend very sensitively on the orientation of the crystal relative to the surface-projected direction of the incident projectile beam. Analogous conclusions were drawn from theoretical investigations of the neutralization of hydrogen anions near Cu(111) and Cu(100) surfaces [12], as well as for Pd(111) and Pd(100) surfaces [13]. In a combined theoretical and experimental study [14], the interaction-time dependence of charge transfer in the scattering of H^- on a Cu(111) surface was found to cause a nonmonotonic variation in the final hydrogen anion yields as functions of the collision energy. A surface-specific interaction time dependence and nonmonotonic dependence on the impact velocity of the survival of hydrogen anions near Li(110), Cu(111), and Pd(111) surfaces was also reported in Ref. [15]. It was shown that at low collision velocities (long interaction times) an enhancement of the anion fractions results from the dynamical confinement of the shifted hydrogen affinity level inside the surface projected bulk band gap, while at high impact velocities, an enhancement in the anion yields was traced to efficient electron recapture from transiently occupied image-potential states on the outgoing path of the surface reflected projectiles.

On free-electron-like metal surfaces, such as aluminum, with relatively narrow band gaps, resonant charge transfer is usually described based on a jellium model for the substrate electronic structure [2,16]. However, a theoretical and experimental investigation of the decay of excited image-potential states of Al (100) surfaces [17] points to effects that go beyond the jellium model. While *ab initio* calculations of the surface electronic structure in jellium approximation predict a single broad maximum in the surface density of states at the position of the first image potential state ($i = 1$) [18], the spectrally resolved two-photon photoemission signal displays a Rydberg series of clearly separated image-potential resonances with quantum numbers $i = 2, 3, 4$, and 5, without the lowest image-potential resonance state ($i = 1$). To resolve this apparent discrepancy, Ref. [17] suggested that such nonjellium effects are due to a resonance trapping effect [19].

Motivated by such electronic-structure-dependent effects on charge transfer near metal surfaces, the goal of the present work is to scrutinize theoretical results that reveal velocity-dependent effects in charge transfer during the reflection of hydrogen atoms on an Al(100) surface, and to relate

these effects to details of the substrate-electronic-structure at the level of density-functional theory (DFT). This paper is organized as follows. We outline our theoretical model in Sec. II. In Sec. III, we discuss numerical results for the chemisorption of hydrogen negative ions on an Al(100) substrate (Sec. III A) and electron transfer during the scattering of hydrogen atoms on an Al surface (Sec. III B). Section IV contains our main conclusions. Unless otherwise stated, we use atomic units ($e = \hbar = m_e = 1$) through this work.

II. THEORETICAL MODEL

We describe the projectile motion classically and model the electronic dynamics during the projectile-surface collision within a spinless Newns-Anderson model [20–23] based on the Hamiltonian

$$H(t) = \sum_k \varepsilon_k n_k + \sum \varepsilon_a(t) n_a + \sum_k [V_{ak}(t) c_a^\dagger c_k + \text{H.c.}] + \sum_l \varepsilon_l n_l + \sum_{kl} [V_{kl}(t) c_k^\dagger c_l + \text{H.c.}], \quad (1)$$

which owes its time-dependence to the projectile trajectory $\mathbf{R}(t)$. We determine the classical trajectory by solving Newton's equation of motion for the scattering of the projectile in a superposition of binary Thomas-Fermi-Molière interatomic potentials that are centered at the lattice points of the substrate. The quantum numbers $k = (n, \mathbf{k}_{||})$ designate bound valence and conduction electronic states n of the metal with energies $\varepsilon_{\min} \leqslant \varepsilon_k < 0$ relative to the position of the vacuum energy level $\varepsilon_{\text{vac}} = 0$. $\mathbf{k}_{||}$ is the Bloch crystal momentum of the substrate electrons, and $\varepsilon_{\min}$ specifies the position of the lower edge of the valence band. The energy of the hydrogen affinity level (AL) $\varepsilon_a(t)$ is shifted due to the image-charge interaction with the metal surface. V_{ak} are the matrix elements for the hydrogen anion formation (defined further below).

The continuum of bound negative-energy substrate states interacts via couplings V_{lk} with a band of delocalized and ionized positive-energy metal states $|l\rangle = |n', \mathbf{k}'_{||}\rangle$ of energies $0 \leqslant \varepsilon_l \leqslant \varepsilon_{\max}$, where $\varepsilon_{\max}$ specifies the high-energy cutoff used in our computation of the hydrogen negative-ion fraction. The continuum-continuum interaction between these states can be neglected if the excitation into positive-energy states is suppressed during the collision. In this case the Hamiltonian (1) reduces to the Newns-Anderson model for a discrete level interacting with one continuum of negative-energy metal states [23].

Since the AL is not directly coupled to positive-energy substrate states, it is convenient to introduce a common index $s \in (a,l)$. The electron annihilation operators c_k and $c_s \in \{c_a, c_l\}$ are subject to the canonical anticommutation relations

$$\{c_k, c_s^\dagger\} = 0, \quad \{c_k, c_{k'}^\dagger\} = \delta_{kk'}, \quad \{c_s, c_{s'}^\dagger\} = \delta_{ss'}. \quad (2)$$

In the Heisenberg picture the equations of motion are now given by

$$i\frac{dc_k}{dt} = [c_k, H] = \varepsilon_k c_k + \sum_s V_{ks}(t) c_s,$$
$$i\frac{dc_s}{dt} = [c_s, H] = \varepsilon_s(t) c_s + \sum_k V_{sk}(t) c_k, \quad (3)$$

subject to the initial conditions $c_k(t_0) = c_k^0$ and $c_s(t_0) = c_s^0$, where t_0 is an arbitrary, but fixed, time long before the collision. Integrating out the negative-energy metal states gives

$$c_k(t) = c_k^0 e^{-i\varepsilon_k(t-t_0)} - i\sum_s \int_{t_0}^t dt' e^{-i\varepsilon_k(t-t')} V_{ks}(t') c_s(t') \quad (4)$$

and results in the equations of motion

$$i\frac{dc_s}{dt} = \varepsilon_s(t) c_s + \sum_{s'} \int dt' \sigma_{ss'}(t,t') c_{s'}(t') + \Phi_s(t). \quad (5)$$

These include a retarded off-diagonal electronic self-energy kernel that accounts for indirect interactions between s states due to their coupling to intermediate bound metal states,

$$\sigma_{ss'}(t,t') = -i\theta(t-t') \sum_k V_{sk}(t) e^{-i\varepsilon_k(t-t')} V_{ks'}(t'), \quad (6)$$

and inhomogeneous terms,

$$\Phi_s(t) = \sum_k c_k^0 e^{-i\varepsilon_k t} V_{sk}(t), \quad (7)$$

that describe direct tunneling transitions from negative-energy metal states. The solutions of Eq. (5) can be expressed in terms of the transition amplitudes $S_{ss'}$ and S_{sk} as

$$c_s(t) = \sum_{s'} S_{ss'}(t,t_0) c_{s'}^0 + \sum_k S_{sk}(t,t_0) c_k^0. \quad (8)$$

The amplitudes for hydrogen negative-ion formation $\{S_{ak}\}$ are given by a system of uncoupled integro-differential Volterra equations,

$$i\frac{dS_{ak}}{dt} = \varepsilon_a(t) S_{ak}(t) + \int dt' \Sigma_{aa}(t,t') S_{ak}(t') + W_{ak}(t), \quad (9)$$

subject to the initial conditions $\{S_{ak}(t_0,t_0) = 0\}$, the matrix elements for anion formation,

$$W_{ak}(t) = \int_{t_0}^t dt' \epsilon^{-1}(t,t') V_{ak}(t'), \quad (10)$$

the self-energy kernel for tunneling into and out of the AL,

$$\Sigma_{aa}(t,t') = \int_{t'}^t d\tau \epsilon^{-1}(t,\tau) \sigma_{aa}(\tau,t'), \quad (11)$$

and the "dielectric" kernel,

$$\epsilon(t,t') = \delta(t-t') - \int dt'' \Pi_0(t,t'') \sigma_{aa}(t'',t'). \quad (12)$$

The integral kernel is defined in terms of the propagator in the subspace of positive-energy states,

$$\Pi_0(t,t') = -i\sum_l \gamma_l(t) e^{-i\varepsilon_l(t-t')} \gamma_l^*(t'), \quad (13)$$

and coupling parameters $\gamma_l(t) = u_l(t)/u_a(t)$ arising from the separability of the couplings $V_{sk} = u_s^*(t) V_k(t)$ (cf. section labeled "Effective one-electron potential" below). The inverse integral kernel in (10) and (11) is determined by the solution of the integral equation

$$\int dt'' \epsilon(t,t'') \epsilon^{-1}(t'',t') = \delta(t-t'). \quad (14)$$

It describes the modification of interaction between the AL and the continuum of negative-energy states due to electronic

transitions into and out of intermediate positive-energy metal states. Details for the derivation of the equations of motion (9) are given in the Appendix.

The hydrogen negative-ion fraction at time t is given by

$$n_a(t) = \langle c_a^\dagger(t) c_a(t)\rangle = \sum_k n_k^0 |S_{ak}(t,t_0)|^2 = \int^{\varepsilon_F} d\varepsilon\, S(\varepsilon,t), \tag{15}$$

where ε_F designates the Fermi energy of the substrate. The initial Fermi-Dirac occupation factors n_k^0 at zero surface temperature are $n_k^0 = \theta(\varepsilon_F - \varepsilon_k)$, such that the time-dependent tunneling density of states (TDOS) projected onto the hydrogen AL becomes

$$S(\varepsilon,t) = \sum_k |S_{ak}(t)|^2 \delta(\varepsilon - \varepsilon_k). \tag{16}$$

A. Effective one-electron potential

To specify the one-electron energy levels ε_k, ε_l, and ε_a and coupling constants V_{ak} and V_{kl}, we base our approach on an effective time-dependent Hamiltonian for the motion of one electron in the electric field of the substrate ionic cores and the neutral hydrogen core of the projectile,

$$h(t) = -\tfrac{1}{2}\nabla_{\mathbf{r}}^2 + v_T(\mathbf{r}) + v_P(\mathbf{r} - \mathbf{R}(t)) + v_{ee}[n_0;\mathbf{r}]. \tag{17}$$

It includes the active electron's kinetic energy (first term), the effective target potential v_T, and the time-dependent projectile model potential v_P and accounts for electronic correlation by a static mean-field potential v_{ee} evaluated with the equilibrium charge-density distribution n_0 of the Al(100) surface. Equation (17) does not account for the time-dependent screening of the ion-surface interaction. This can be justified if the substrate electrons do not have enough time to redistribute and screen the electric field of the projectile. The typical time interval over which the external perturbation is screened by the substrate is given by the inverse surface plasma frequency $\tau_0 = 2\pi/\sqrt{2\pi\bar{n}} \approx 15$ of the Al substrate with an average bulk electron density $\bar{n} \approx 0.03$. If τ_0 is much larger than the characteristic time for resonant charge transfer, the substrate electron distribution has not enough time to adjust to the rapid projectile charge changes and remains close to its equilibrium distribution n_0. In the opposite limit of slow adsorbate charge fluctuations, the substrate electron distribution follows almost instantaneously the projectile charge state, and the effective electron potential has to include a dynamical screening correction $\delta v_{ee}(\mathbf{r},t)$ [24]. For the collision energies explored by the experiment in Refs. [1,2], we find that an approximation based on the static electron potential $v_{ee}[n_0;\mathbf{r}]$ is able to provide good quantitative agreement with measured hydrogen anion yields on Al surfaces.

The equilibrium substrate charge-density distribution n_0 and effective screened one-electron potential,

$$v_s(\mathbf{r}) = v_T(\mathbf{r}) + v_{ee}[n_0;\mathbf{r}], \tag{18}$$

are obtained within the framework of DFT, based on the Thomas-Fermi-von-Weizsäcker approximation [25,26]. The mean-field correlation potential

$$v_{ee}(\mathbf{r}) = \int d^3\mathbf{r}' \frac{n_0(\mathbf{r}')}{|\mathbf{r} - \mathbf{r}'|} + v_{\rm xc}[n_0;\mathbf{r}] \tag{19}$$

consists of the local Hartree (first term) and an exchange-correlation potential (second term). We employ the local-density approximation (LDA) for the effective exchange and correlation potential, using the Dirac approximation [27] for the exchange and the Wigner approximation [28] for the correlation energy of the electron gas,

$$v_{\rm xc}[n_0;\mathbf{r}] \approx v_{\rm xc}^{\rm LDA}(n_0(\mathbf{r})) = \frac{d}{dn}[n\varepsilon_{\rm xc}(n)]|_{n=n_0(\mathbf{r})}, \tag{20}$$

where the exchange-correlation energy per electron,

$$\varepsilon_{\rm xc}(n) = -\frac{0.458}{r_s} - \frac{0.44}{r_s + 7.8}, \tag{21}$$

is expressed in terms of the screening radius $r_s = (3/4\pi n)^{1/3}$. Since the LDA assumes that the electron potential at a point $\mathbf{r}$ is determined by the local charge density at that point, the approximation in (20) neglects nonlocal effects of the electronic self-image interaction. The correct electronic potential merges into the image potential at large distances to the surface,

$$v_{ee}(\mathbf{r}) \to v_{\rm im}(z) = -\frac{1}{4(z - z_{\rm im})}, \quad z \to \infty, \tag{22}$$

where $z_{\rm im}$ specifies the position of the image-charge plane defined as the first moment of the charge distribution on the substrate induced by an external uniform electric field [29]. Since our LDA-based approach does not include nonlocal image-charge effects, we ascertain the correct limit of (22) by downshifting the energy of the AL (see below).

The unscreened target potential of the substrate ionic cores

$$v_T(\mathbf{r}) = \sum_t w_{\rm ps}(|\mathbf{r} - \mathbf{R}_t|) \tag{23}$$

is represented by a superposition of ionic model potentials

$$w_{\rm ps}(r) = -\frac{z}{B}\left\{\frac{1}{x}[1 - (1 + bx)e^{-ax}] - Ae^{-x}\right\}. \tag{24}$$

These are centered at the substrate lattice points $\{\mathbf{R}_t\}$ and include as parameters the valence charge of the Al ionic cores $z = 3$, $x = r/B$, $b = (a^3 - 2a)/4(a^2 - 1)$, $A = a^2 - 2b$, $a = 3.573$, and $B = 0.317$ [30]. The equilibrium charge distribution $n_0(\mathbf{r})$ on the Al(100) surface is shown in Fig. 1(a) and the corresponding screened potential $v_s(\mathbf{r}) = v_T(\mathbf{r}) + v_{ee}(\mathbf{r})$ in Fig. 1(b). As a consequence of the Pauli exclusion principle, valence electrons avoid getting close to target ionic cores and redistribute laterally. The screened potential $v_s(\mathbf{r})$ converges to the vacuum energy level at large distances from the surface.

The projectile potential is modeled by a regularized zero-range Fermi s-wave pseudopotential [31],

$$v_P(\mathbf{r}) = \frac{2\pi}{\alpha}\delta^{(3)}(\mathbf{r})\frac{\partial}{\partial r}r, \tag{25}$$

with a single parameter α that is adjusted such that the undistorted projectile Hamiltonian $h_P = -\frac{1}{2}\nabla^2 + v_P$ reproduces

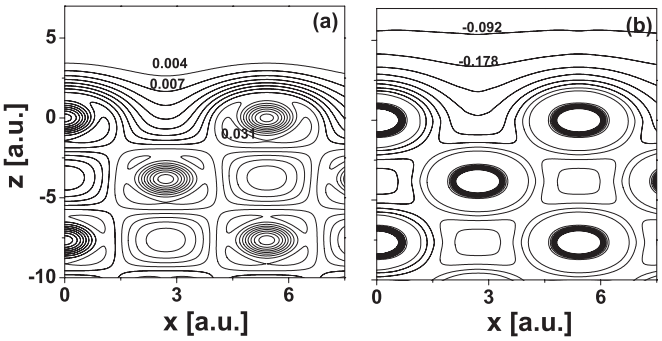

FIG. 1. Contour map of the (a) equilibrium charge-density distribution $n_0(\mathbf{r})$ of valence electrons and (b) potential energy $v_s(\mathbf{r})$ for an electron near the Al(100) surface. The x axis is oriented along the [011] crystal-surface direction and the z axis along the [100] crystal-surface direction. The contour-line spacing is 0.003 a.u. in (a) and −0.086 a.u. in (b).

the affinity $\varepsilon_a^0 = -\alpha^2/2 = -0.75$ eV of the hydrogen anion,

$$h_P|a\rangle = -\frac{\alpha^2}{2}|a\rangle. \tag{26}$$

We diagonalize the metal Hamiltonian $h_T = -\frac{1}{2}\nabla^2 + v_s$ in terms of Bloch eigenstates,

$$h_T|n\mathbf{k}_{||}\rangle = \varepsilon_n(\mathbf{k}_{||})|n\mathbf{k}_{||}\rangle, \tag{27}$$

of energies $\varepsilon_n(\mathbf{k}_{||})$ and parallel crystal momenta $\mathbf{k}_{||}$ in the first surface Brillouin zone (SBZ). The SBZ and the high-symmetry directions of the crystal are indicated in Fig. 2(a). The irreducible part of SBZ is a triangle connecting by straight lines the points $\bar{\Gamma}$, $\bar{X}$, and $\bar{M}$ in momentum space. The band structure $\varepsilon_n = \varepsilon_n(\mathbf{k}_{||})$ supported by the screened surface potential $v_s(\mathbf{r})$ is shown in Fig. 2(b). The almost parabolic dispersion relations in the distribution of substrate energy levels for the highest shown energies indicate free-electron character. Avoided crossings of target energy levels along the

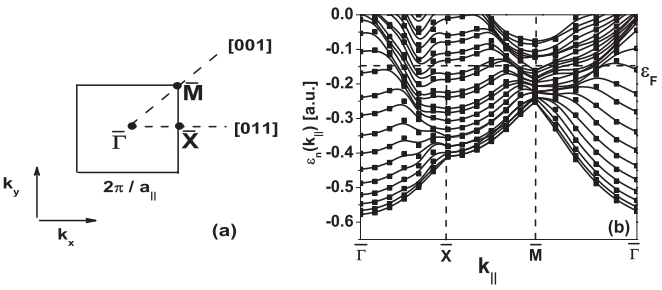

FIG. 2. (a) Surface Brillouin zone (SBZ) for the unreconstructed Al(100) surface with the three high-symmetry end points $\bar{\Gamma}$, $\bar{X}$, and $\bar{M}$. The main crystallographic directions are along $\bar{\Gamma}\bar{X}$ ([011]) and $\bar{\Gamma}\bar{M}$ ([001]). The edge length of the square Brillouin zone is $2\pi/a_{||} = 1.16$ a.u., where $a_{||} = a_0/\sqrt{2} = 5.41$ a.u. is the lattice spacing between Al ionic cores along the [011] direction. The Cartesian coordinates of the high-symmetry points are $\bar{\Gamma} = (0.00,0.00)$, $\bar{X} = (0.58,0.00)$, and $\bar{M} = (0.58,0.58)$. (b) Band structure $\varepsilon_n = \varepsilon_n(\mathbf{k}_{||})$ of the Al(100) surface on a triangle in the SBZ. The crystal momentum $\mathbf{k}_{||}$ is varied along straight lines connecting the end points $\bar{\Gamma}$, $\bar{X}$, and $\bar{M}$.

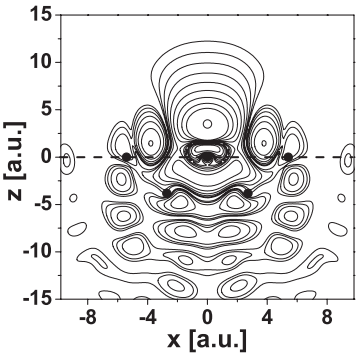

FIG. 3. Probability density of the orthogonalized AL orbital near an Al(100) surface. The position of the first surface layer $z = 0$ is indicated by the dashed line. The projectile (open circle) is at the distance $D = 3.5$ a.u. in front of the first surface layer and on top of an Al-ionic core. The positions of a few substrate ionic cores in the first and second surface layers are indicated as dots. The x axis is oriented along the [011] direction and the z axis along the [100] direction.

$\bar{\Gamma}\bar{X}$ and $\bar{\Gamma}\bar{M}$ crystal-surface directions cause deviations from the free-electron behavior.

For each fixed projectile position $\mathbf{R}(t)$ we Gram-Schmidt orthogonalize the AL to negative-energy metal states according to

$$|a(\mathbf{R}(t))\rangle = A_0^{-1/2}\left(|a_0(\mathbf{R}(t))\rangle - \sum_k |k\rangle\langle k|a_0(\mathbf{R}(t))\rangle\right), \tag{28}$$

where the renormalization constant $A_0(t \to \pm\infty) = 1$ is given by

$$A_0(t) = 1 - \int_{\varepsilon_{\min}}^{\varepsilon_{\rm vac}} d\varepsilon \rho_{\rm AL}^0(\varepsilon,t). \tag{29}$$

The undistorted AL wave function in the rest frame of the surface is

$$\langle\mathbf{r}|a_0(\mathbf{R}(t))\rangle = \sqrt{\frac{\alpha}{2\pi}}\frac{e^{-\alpha|\mathbf{r}-\mathbf{R}(t)|}}{|\mathbf{r}-\mathbf{R}(t)|}, \tag{30}$$

and

$$\rho_{\rm AL}^0(\varepsilon,t) = \sum_k |\langle a_0(\mathbf{R}(t))|k\rangle|^2\delta(\varepsilon-\varepsilon_k) \tag{31}$$

is the density of unperturbed metal states projected onto the AL. $\{\langle a_0(\mathbf{R}(t))|k\rangle\}$ are overlap integrals. The charge-density distribution $|\langle\mathbf{r}|a(\mathbf{R})\rangle|^2$ near the Al(100) surface is shown in Fig. 3 for a projectile positioned on top of an Al-ionic core at $\mathbf{R} = (0,0,D)$ at the distance $D = 3.5$ from the surface. The spherical symmetry of the bare AL orbital is distorted and exhibits a directional character due to hybridization with substrate Bloch orbitals. Bonding charge accumulates in between the projectile and the nearest Al ionic core, and a nodal structure emerges in a direction normal to the surface. The probability distribution protrudes on the lateral sides of the projectile. It exhibits nodes in the interstitial region between the nearest three Al cores in the first surface layer.

We identify the parameters ε_k with the eigenenergies of the negative-energy metal states $\varepsilon_k = \varepsilon_n(\mathbf{k}_{||}) < 0$ and $\varepsilon_l = \varepsilon_n(\mathbf{k}_{||}) \geqslant 0$ with positive-energy metal states. The

couplings-matrix elements for the projectile potential are

$$V_{ak}(t) = \langle a(t)|v_P(t)|n\mathbf{k}_{||}\rangle\theta(-\varepsilon_n(\mathbf{k}_{||})) \tag{32}$$

and

$$V_{lk}(t) = \langle n'\mathbf{k}'_{||}|v_P(t)|n\mathbf{k}_{||}\rangle\theta(-\varepsilon_n(\mathbf{k}_{||}))\theta(\varepsilon_{n'}(\mathbf{k}'_{||})). \tag{33}$$

These matrix elements are separable in the zero-range model (25), e.g.,

$$\langle n'\mathbf{k}'_{||}|v_P(t)|n\mathbf{k}_{||}\rangle = \frac{2\pi}{\alpha}\varphi^*_{n',\mathbf{k}'_{||}}(\mathbf{R}(t))\varphi_{n,\mathbf{k}_{||}}(\mathbf{R}(t)). \tag{34}$$

The substrate Bloch wave functions evaluated at the position of the projectile $\mathbf{R}(t) = (\mathbf{R}_{||}(t), D(t))$ are

$$\varphi_{n,\mathbf{k}_{||}}(\mathbf{R}(t)) = \sum_{\mathbf{G}_{||}} c_{n,\mathbf{G}_{||}+\mathbf{k}_{||}}[D(t)]e^{i(\mathbf{G}_{||}+\mathbf{k}_{||})\cdot\mathbf{R}_{||}(t)}. \tag{35}$$

$D(t)$ is the ion-surface distance, $\mathbf{R}_{||}(t)$ is the surface-projected collision trajectory, and $\{\mathbf{G}_{||}\}$ are the substrate reciprocal lattice vectors. In our numerical applications we approximate the matrix element for anion formation as

$$\begin{aligned}\langle a(t)|v_P(t)|n\mathbf{k}_{||}\rangle &\approx \langle a(t)|a_0(t)\rangle\langle a_0(t)|v_P|n\mathbf{k}_{||}\rangle \\ &= [2\pi\alpha A_0(t)]^{1/2}\varphi_{n,\mathbf{k}_{||}}(\mathbf{R}(t)).\end{aligned} \tag{36}$$

The projectile level shift,

$$\varepsilon_a(t) = \langle a(t)|h(t)|a(t)\rangle \approx A_0(t)\left[\varepsilon_a^0 + \langle a_0(t)|v_s|a_0(t)\rangle\right], \tag{37}$$

tracks the surface potential and is weakened due to orbital orthogonalization, accounted for by the renormalization constant $0 < A_0 \leqslant 1$. We approximate $\varepsilon_a(t)$ by the static downshift of the AL due to the image-charge attraction,

$$\varepsilon_a(t) \approx A_0(t)\left[\varepsilon_a^0 + \langle a_0(t)|v_{\rm im}|a_0(t)\rangle\right], \tag{38}$$

using the semiclassical approximation for the static image potential $v_{\rm im}(z)$ of Ref. [32]. Note that this approximation implies positive dispersion of the surface plasmon at long wavelengths, while negative dispersion [33] yields the correct asymptotic form (22) of the image potential. In our numerical application, however, we find, that this change in the surface plasmon dispersion relation has a negligible effect on the final anion fractions.

III. NUMERICAL RESULTS AND DISCUSSION

We model the unreconstructed Al(100) surface as a slab with a thickness of 10 bulk lattice constants $a_0 = 7.653$ [34]. The unit supercell consists of 9 layers of Al ionic cores plus a vacuum region on top of both surfaces of the Al slab. The interlayer spacing is $a_0/2$. The vacuum region on both surfaces of the crystal has a thickness of 6 layers. We numerically solve the equations of motion (9) by using a uniform momentum space mesh with spacings $\Delta k_x = \Delta k_y = 0.145$, $-\sqrt{2}\pi/a_0 \leqslant k_x \leqslant \sqrt{2}\pi/a_0$, and $-\sqrt{2}\pi/a_0 \leqslant k_y \leqslant \sqrt{2}\pi/a_0$. We include 50 substrate bands and thus $50 \times 81 = 4050$ electronic states. We use equidistant time steps $\delta t = 0.25$ for the numerical integration of the equations of motion in order to obtain converged anion yields.

A. Results in fixed-ion approximation

In fixed-ion approximation, the equations of motion (9) [see also Eqs. (A1) and (A2) in the Appendix] can be solved by Fourier transformation. The occupation number of the hydrogen AL,

$$n_a = \int_{-\infty}^{\varepsilon_F} d\varepsilon\rho_a(\varepsilon), \tag{39}$$

can be expressed in terms of the projected density of states (PDOS),

$$\rho_a(\varepsilon) = -\frac{1}{\pi}{\rm Im}G_{aa}(\varepsilon), \tag{40}$$

where

$$G_{aa}(\varepsilon) = \frac{1}{\varepsilon - \varepsilon_a - \Sigma_{aa}(\varepsilon)} \tag{41}$$

is the Green's function of the distorted AL. The complex poles of $G_{aa}(\varepsilon)$ at $\varepsilon = E_R - i\Gamma_R/2$ on the second Riemann sheet of the complex energy correspond to resonance states of the adsorbate system. The width Γ_R is related to the lifetime of the electronic states near the surface due resonant charge transfer $\tau_R = \Gamma_R^{-1}$. $G_{aa}(\varepsilon)$, in turn, is given by the renormalized self-energy function of the AL,

$$\Sigma_{aa}(\varepsilon) = \frac{\sigma_{aa}(\varepsilon)}{\epsilon(\varepsilon)}, \tag{42}$$

which is expressed in terms of the zeroth-order self-energy function, excluding indirect interactions of the AL with the continuum of ionized metal states,

$$\sigma_{aa}(\varepsilon) = \Lambda_0(\varepsilon) - i\Delta_0(\varepsilon). \tag{43}$$

The imaginary and real parts of σ_{aa} represent the energy-dependent hybridization width

$$\Delta_0(\varepsilon) = \pi\sum_k |V_{ak}|^2\delta(\varepsilon - \varepsilon_k) \tag{44}$$

and chemisorption shift

$$\Lambda_0(\varepsilon) = \frac{1}{\pi}{\rm P}\int d\varepsilon'\frac{\Delta_0(\varepsilon')}{\varepsilon - \varepsilon'}. \tag{45}$$

The "dielectric function"

$$\epsilon(\varepsilon) = 1 - \Pi_0(\varepsilon)\sigma_{aa}(\varepsilon) \tag{46}$$

is the Fourier transform of the integral kernel (12). In fixed-ion approximation it depends parametrically on the projectile-surface distance D. It expresses the effect of AL couplings to the continuum of positive-energy metal states and is defined in terms of the propagator in the space of ionized substrate states,

$$\Pi_0(\varepsilon) = \sum_l \frac{|\gamma_l|^2}{\varepsilon - \varepsilon_l + i0}. \tag{47}$$

The PDOS $\rho_a^0(\varepsilon)$, calculated without including direct continuum-continuum transitions (i.e., for $V_{lk} = 0$), is shown in Fig. 4(a) for fixed distances D relative to the position of the first Al layer. The lateral position of the adsorbate atom is fixed on top of an Al ionic core. The center energy $E_{\rm AL}^0$ and width $\Gamma_{\rm AL}^0$ of the AL-resonance distribution are extracted by

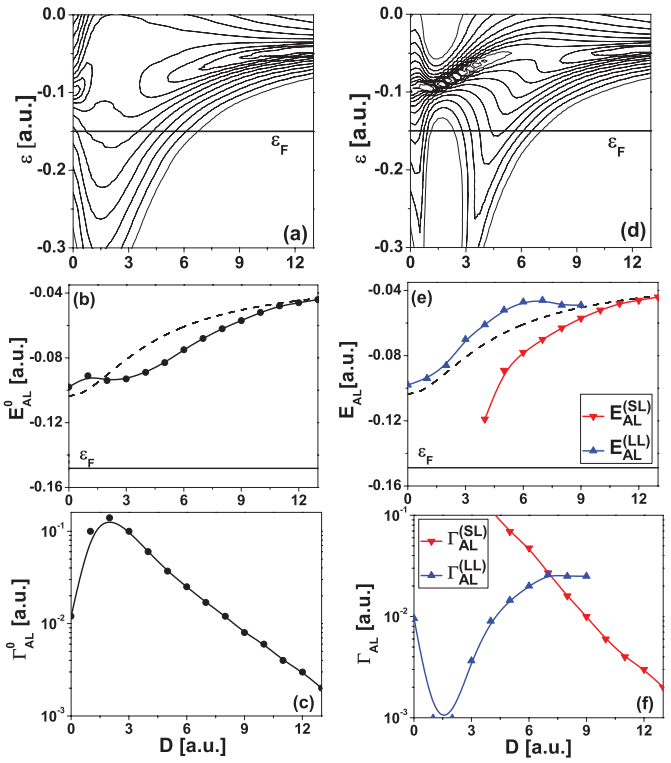

FIG. 4. (Color online) (a) Density of states $\rho_a^0(\varepsilon, D)$ projected onto the H^- AL interacting with an Al(100) surface in fixed-ion approximation. Virtual transitions to the continuum of ionized metal states are neglected. (b) Energy E^0_{AL} and (c) decay width Γ^0_{AL} of the AL resonance in fixed-ion approximation. (d) Density of states $\rho_a(\varepsilon, D)$ projected onto hydrogen AL interacting with an Al(100) surface in fixed-ion approximation. Virtual transitions to the continuum of ionized metal states are included. The energy $E^{(LL)}_{AL}$ and level width $\Gamma^{(LL)}_{AL}$ of the long-lived AL resonance are indicated by the upward pointing triangles in (e) and (f), respectively. The energy $E^{(SL)}_{AL}$ and decay width $\Gamma^{(SL)}_{AL}$ of the short-lived AL resonance are given by the inverted triangles. The position of the Fermi level is indicated by the solid line in (a), (b), (d), and (e). The dashed curve in (b) and (e) shows the image-potential-shifted energy of the H^- AL $\varepsilon_a(D)$.

fitting the Breit-Wigner resonance profile,

$$\rho_a^0(\varepsilon, D) \approx \frac{1}{\pi} \frac{\Gamma^0_{AL}(D)}{\left[\varepsilon - E^0_{AL}(D)\right]^2 + \left[\Gamma^0_{AL}(D)/2\right]^2}, \tag{48}$$

to the numerically calculated PDOS. At large distances $D > 7$, corresponding to weak interactions of the AL with the substrate, the distribution is narrow [Fig. 4(a)], and its center shifts downwards towards valence bands. The AL follows the image potential variation $E^0_{AL} \approx \varepsilon_a^0 - 1/4D$ [Fig. 4(b)]. However, the interaction with the conduction band (which has width of ≈4 eV) induces an additional small hybridization shift that lowers the AL in energy. The width of the resonance distribution is due to irreversible electron loss from the AL into unoccupied conduction-band states. At such large distances, the AL resonance is long-lived with lifetime $\tau_{AL} = (\Gamma^0_{AL})^{-1} \approx$ 100 that decreases exponentially with decreasing D.

At smaller distances $D \approx 5$, the center of the AL-resonance distribution shifts to lower energies and moves toward the valence band, once E^0_{AL} shifts ≈1 eV above the Fermi level. The hybridization interaction with conduction and valence bands has broadened the AL-resonance distribution to a width of $\Gamma^0_{AL} \approx 1$ eV. This is sufficient to enable electron capture from the valence band so that the AL becomes partially occupied.

At even smaller distances $D < 4$, the AL interacts with a large spectral range of valence- and conduction-band states. This dramatically reduces the AL-resonance lifetime to $\tau_{AL} \approx$ 10. The AL shift [Fig. 4(b)] and width [Fig. 4(c)] closely follow the variation predicted from the jellium model for the surface electronic structure. For instance, the AL width near jelliumlike Al(111) surfaces, as reported in [35], is $\Gamma_{AL} >$ 1 eV at small distances to the surface, in good quantitative agreement with our result. However, deviations from the jellium model occur at short distances, $D \leqslant 2$, since the PDOS becomes narrower due the decrease of the surface density of states in the classically forbidden region of the surface potential $v_s(\mathbf{r})$ near the repulsive Al ionic cores [cf. Fig. 1(b)]. Thus, the exponential increase of the AL width is truncated at small distances and becomes largest at $D \approx 1.5$.

When the indirect interaction of the AL with the continuum of ionized metal states is accounted for, the PDOS $\rho_a(\varepsilon, D)$ changes relative to ρ_a^0, as shown in Fig. 4(d). The position and the width of the resonance levels in the adsorbate system are determined by fitting a superposition of overlapping Breit-Wigner resonance profiles,

$$\rho(\varepsilon) = \sum_R \frac{A_R}{\pi} \frac{\Gamma_R}{(\varepsilon - E_R)^2 + (\Gamma_R/2)^2}, \tag{49}$$

to the PDOS, where A_R are weight factors. At large distances $D > 7$, the distribution exhibits a narrow resonance structure in the conduction band, corresponding to a state that correlates asymptotically to the undistorted hydrogen affinity. In the strong-coupling region $5 < D < 7$, hybridization of the AL with the continuum of ionized metal states changes the PDOS: The short-lived AL-resonance state shifts downward toward the valence band more rapidly [Fig. 4(e)], its spectral weight in the PDOS progressively decreases, and its decay width Γ^{SL}_{AL} increases exponentially as D decreases [Fig. 4(f)].

At smaller distances $D \in [4,5]$, the short-lived AL-resonance state has a lifetime of $\tau^{SL}_{AL} < 10$ and becomes indistinguishable in the PDOS. At the same time, a long-lived resonance state emerges in the PDOS and moves into resonance with unoccupied conduction-band states [Figs. 4(e) and 4(f)]. It exhibits a repulsive interaction with the conduction band, since its energetic position $E^{LL}_{AL}(D)$ moves upward relative to the position of the image-potential-shifted AL. This resonance state has a large amplitude and becomes increasingly important in the PDOS for decreasing D [Fig. 4(d)]. Its decay width $\Gamma^{LL}_{AL}(D)$ decreases with decreasing D due to the suppression of electron loss to the conduction band [Fig. 4(e)]. Thus, in the region of strong coupling to the substrate, $D < 7$, this resonance state is long-lived with a lifetime of $\tau^{LL}_{AL} > 50$. At $D \approx 2$, the AL-resonance distribution becomes very narrow. Its width decreases significantly to $\Gamma^{LL}_{AL} = 0.01$ eV. It is worth noting that the variation of the AL widths with D in Fig. 4(e) is reminiscent of the resonance trapping effect in the dynamics of interacting resonance states, which

increases the lifetimes of certain resonances for increasing coupling strength to the continuum [36].

The reduction of the decay width $\Gamma_{\rm AL}^{\rm LL}$ of the long-lived AL-resonance state at small distances can be interpreted as due to the destructive interference of tunneling amplitudes into and out of the AL by rewriting the effective self-energy function (42) as

$$\Sigma_{aa}(\varepsilon) = \sigma_{aa}(\varepsilon) + \sigma_{aa}(\varepsilon)\frac{\Pi_0(\varepsilon)}{1-\Pi_0(\varepsilon)\sigma_{aa}(\varepsilon)}\sigma_{aa}(\varepsilon). \qquad (50)$$

The first term is the electron self-energy due to resonant transitions into and out of negative-energy metal states. The second contribution is due to tunneling into and out of positive-energy metal states. For strong coupling of the AL to the continuum of ionized states, $|\Pi_0\sigma_{aa}| \gg 1$, the contributions of the two alternative paths for electron tunneling are comparable and cancel, such that the self-energy function approximately vanishes, $\Sigma_{aa}(\varepsilon) \approx 0$, whenever the position-dependent hybridization factor $\epsilon(\varepsilon)$ (46) diverges. In this case interactions of the AL with positive-energy metal states suppress electron loss into the conduction band, promoting the formation of the long-lived AL resonance.

To analyze these results further, we compare the AL-level shift (45) and width (44) with the renormalized energy-dependent shift $\Lambda = {\rm Re}\Sigma_{aa}$ and width $\Delta = -{\rm Im}\Sigma_{aa}$ in Figs. 5(a) and 5(b) at the fixed distance $D = 4$. The major effect of the coupling to the continuum of ionized metal states

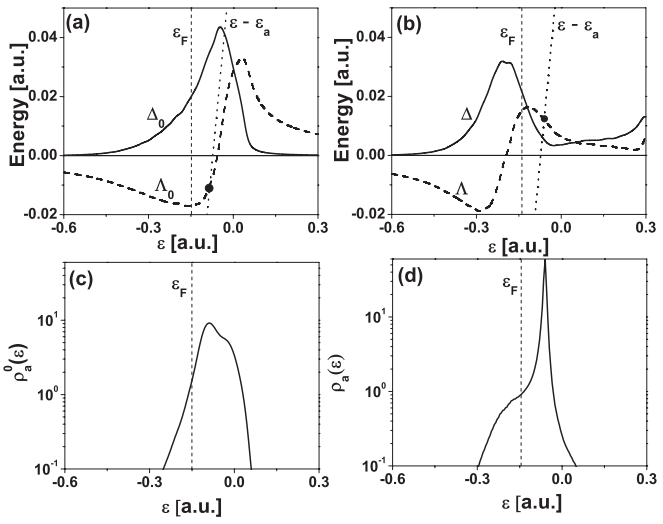

FIG. 5. (a) Chemisorption shift $\Lambda_0(\varepsilon)$ (45) and width $\Delta_0(\varepsilon)$ (44) functions for the H^- AL near an Al(100) surface in fixed-ion approximation. The ion-surface distance is $D = 4$ a.u.. Virtual transitions to the continuum of ionized metal states are neglected. (b) Renormalized chemisorption shift $\Lambda(\varepsilon) = {\rm Re}\Sigma_{aa}$ and width $\Delta(\varepsilon) = -{\rm Im}\Sigma_{aa}$ functions for the hydrogen AL resonance including virtual transitions to the continuum of ionized metal. The dot in (a) and (b) indicates the approximate energy of the hydrogen AL resonance, as determined by solutions of the equation $\varepsilon - \varepsilon_a = \Lambda_0(\varepsilon)$ and by $\varepsilon - \varepsilon_a = \Lambda(\varepsilon)$, respectively. The dashed lines in (a) and (b) specify the position of the Fermi level $\varepsilon_F = -0.15$ a.u.. The dotted straight lines in (a) and (b) indicate the transition frequencies $\varepsilon - \varepsilon_a$. Panels (c),(d) give the unperturbed $\rho_a^0(\varepsilon)$ and renormalized $\rho_a(\varepsilon)$ densities of states projected onto the hydrogen AL, respectively.

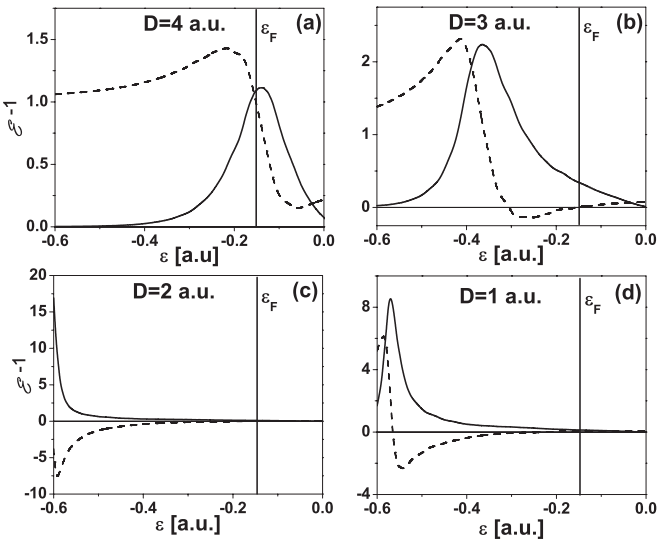

FIG. 6. Inverse dielectric function $\epsilon^{-1}(\varepsilon)$ for the H^- AL near an Al(100) surface in fixed-ion approximation. The ion-surface distance is (a) $D = 4$ a.u., (b) 3 a.u., (c) 2 a.u., and (d) 1 a.u.. The real and imaginary parts of the distribution are indicated by the dashed and solid lines, respectively. The vertical solid line indicates the position of the Fermi level $\varepsilon_F = -0.15$.

is the redistribution in the density of states across the Fermi level. This redistribution induces a repulsive interaction of the AL with the valence band, such that the AL remains energetically localized above the upper edge of the band [Fig. 5(b)]. Due to the decrease of the surface density of states above the upper edge of the valence band, electron loss becomes unlikely, such that this resonance state becomes long-lived and gains anion character with a corresponding large amplitude in the PDOS [Fig. 5(d)]. In contrast, the undistorted hybridization interaction with the metal $\sigma_{aa}(\varepsilon)$ exhibits much weaker energy dependence. It leads to the formation of a short-lived AL resonance due to efficient electron loss into the conduction band [Fig. 5(c)].

Additional details on the indirect interaction of the AL with the continuum of positive-energy metal states are contained in the inverse dielectric function $\epsilon^{-1}(\varepsilon)$ (46) and shown in Fig. 6 for fixed ion-surface distances $D = 1, 2, 3$, and 4. Both, the real and imaginary part of $\epsilon^{-1}(\varepsilon)$ change exponentially with D and track the variation of the static surface potential $v_s(\mathbf{r})$ in direction normal to the surface. The finite width of the distribution localizes the strength of the charge-transfer coupling to occupied valence-band states and makes electron tunneling to unoccupied conduction-band states unlikely.

B. Results for moving ions

1. *Normal incidence*

To decide whether the redistribution in the density of states due indirect interactions of the AL with ionized substrate states affects the time-dependent characteristics of charge transfer at the Al(100) surface, we investigate normally incident projectiles with kinetic energies between 10 eV and 4 keV.

The TDOS $S(\varepsilon,t)$ is shown in Fig. 7 for hydrogen atoms, which collide head-on with an Al-ionic core and reflect as H^-. For slowly moving projectiles with speed $v_n = 0.02$

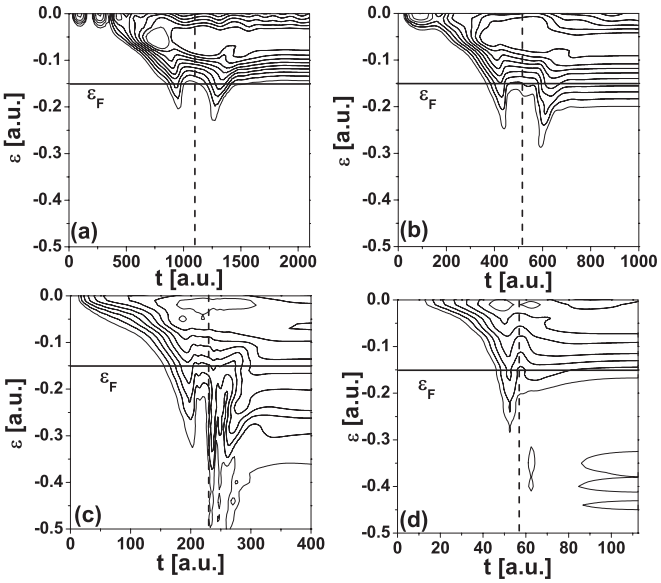

FIG. 7. Time-dependent tunneling density of states $S(\varepsilon,t)$ for hydrogen atoms normally incident on an Al(100) surface and backscattered as H^- with velocities (a) $v_n = 0.02$ (corresponding to a collision energy of 10 eV), (b) 0.045 (50 eV), (c) 0.1 (250 eV), and (d) 0.4 a.u. (4 keV). The time of closest approach to the surface is indicated by the vertical dashed line.

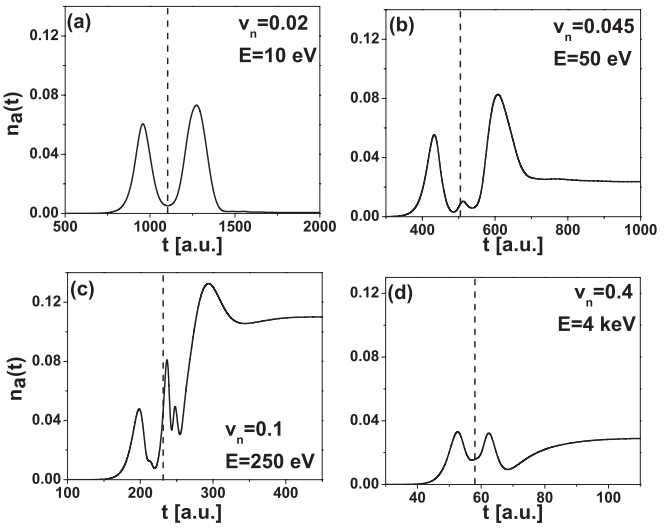

FIG. 8. Transient H^- fractions near an Al(100) surface for normally incident hydrogen atoms with impact velocities (a) $v_n = 0.02$, (b) 0.045, (c) 0.1, (d) 0.4 a.u., and corresponding collision energies E. The time of closest approach to the surface is indicated by the vertical dashed lines.

[corresponding to a kinetic energy of $E = 10$ eV, Fig. 7(a)] and prior to the reflection on the surface, the TDOS closely follows the adiabatic fixed-ion distribution in Fig. 4(d). The density of states concentrates in the conduction band and downshifts toward the Fermi level. A short-lived resonance extends into the low-density tail of the distribution and shifts across the Fermi level, enabling electron capture into the AL. Close to the point of closest approach on the trajectory, redistribution in the TDOS near the Fermi level initiates electron loss due to the formation of the long-lived AL-resonance state that energetically overlaps the conduction band. A similar effect occurs after the reflection. The short-lived AL resonance again shifts downward into the valence band and re-enables electron capture on the exit part of the trajectory. Electron loss restores the neutral equilibrium charge state, such that a negligible negative-ion fraction evolves out of the Fermi sea ($n_a = 0.06\%$).

At the slightly higher impact velocity $v_n = 0.045$, shown in Fig. 7(b), corresponding to a collision energy of 50 eV, the TDOS follows the instantaneous PDOS prior to the reflection from the surface. After the reflection, a velocity-dependent redistribution of states across the Fermi level is evident, which allows the AL to shift into resonance with deeper valence levels and increases the probability for negative-ion formation. Charge equilibration due to subsequent electron loss into the conduction band is delayed, allowing negative-ion formation with significantly larger final anion yields $n_a = 2.7\%$. Thus, hydrogen negative-ion formation on the Al(100) surface depends quite sensitively on the normal component of the exit velocity.

For even more rapid reflection, at $v_n = 0.1$ (corresponding to a collision energy of 250 eV), as shown in Fig. 7(c), a substantial deviation from the fixed-ion results of Fig. 4(d) occurs. Near the point of closest approach the TDOS extends from conduction- into valence-band states, causing efficient promotion of deep valence electrons into resonance with the AL. Since electron loss into the conduction band becomes inefficient after the reflection, H^- formation via resonant electron capture is prominent and leads to further increase of the final negative-ion fraction to $n_a = 11\%$. Finally, at the highest velocity $v_n = 0.4$ (corresponding to a collision energy of 4 keV), the strength of the charge-transfer coupling has weakened substantially, leading to the smaller final fraction $n_a = 2.7\%$ [Fig. 7(d)]. This decrease of the final negative-ion fraction is due to a redistribution in the TDOS, that occurs when the surface density of states shifts to high energies and close to the ionization threshold, thereby reducing the probability for electron capture from valence-band states. Thus, at velocities $v_n > 0.3$ the strength of the charge-transfer coupling weakens, resulting in less efficient negative-ion formation.

The transient negative-ion fractions corresponding to the TDOS in Fig. 7 are shown in Fig. 8. The negative-ion fraction evolves adiabatically at low collision velocities $v_n \leqslant 0.02$. For $0.02 < v_n < 0.1$, the H^- fraction evolves quasi-adiabatically, as electron capture after the reflection is enhanced due to a redistribution in the surface density of states. This enables the AL to shift into resonance with deeper valence states. Near $v_n = 0.1$ electron loss after the reflection is highly suppressed, resulting in large negative-ion yields $n_a > 10\%$. The hydrogen negative-ion fraction attains a maximum of $n_a = 15\%$ near $v_{\max} = 0.13$ and decreases with continued increase of the velocity (Fig. 9). For instance, at $v_n = 0.3$, the anion yield is $n_a = 9\%$. At $v_n = 0.4$ it reduces to less than 3%.

To analyze these results further, the initial-state-resolved momentum distributions for electrons that tunnel from the valence band into the AL,

$$\sigma(a \leftarrow \mathbf{k}_{||}) = \sum_n |S_{a,n\mathbf{k}_{||}}(t \to \infty)|^2 \theta(\varepsilon_F - \varepsilon_n(\mathbf{k}_{||})), \quad (51)$$

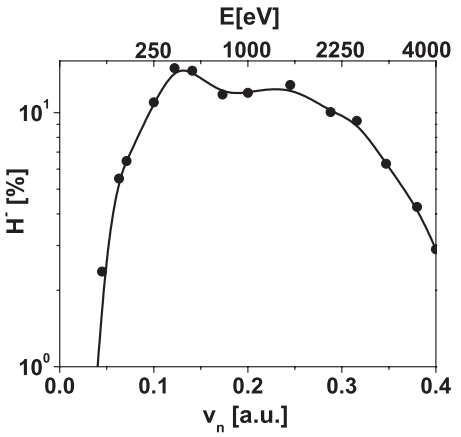

FIG. 9. H^- fraction for H atoms reflected off an Al(100) surface as a function of the exit velocity v_n at normal incidence. The collision energy E is given on the top horizontal axis.

are shown in Fig. 10. The final negative-ion fractions are given by

$$n_a = \int_{\mathrm{SBZ}} \frac{d^2\mathbf{k}_{||}}{(2\pi)^2}\sigma(a \leftarrow \mathbf{k}_{||}). \tag{52}$$

For the relatively high impact velocities in Figs. 10(a) and 10(b), the distributions are peaked near zero parallel momentum and display approximate circular symmetry. Thus, for high collision velocities and short ion-surface interaction times, details of the substrate band structure are blurred, and electrons from low-lying valence levels moving with momenta near the center $\bar{\Gamma}(\mathbf{k}_{||} = \mathbf{0})$ of the SBZ are promoted into the hydrogen AL.

When the projectile impact velocity is decreased below the critical velocity $v_{\max} \approx 0.1$, electron loss after reflection

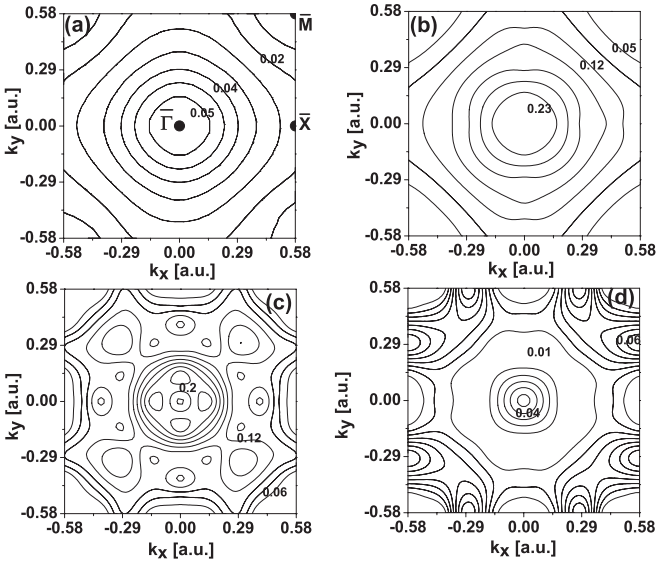

FIG. 10. Initial-state-resolved momentum distributions of valence electrons $\sigma(a \leftarrow \mathbf{k}_{||})$ [Eq. (51)] for normally incident hydrogen atoms backscattered on an Al(100) surface as H^- with exit velocities (a) $v_n = 0.4$, (b) 0.2, (c) 0.1, and (d) 0.045 a.u., corresponding to collision energies $E = 4000$, 1000, 250, and 50 eV, respectively. The three high-symmetry points in the SBZ are indicated in (a).

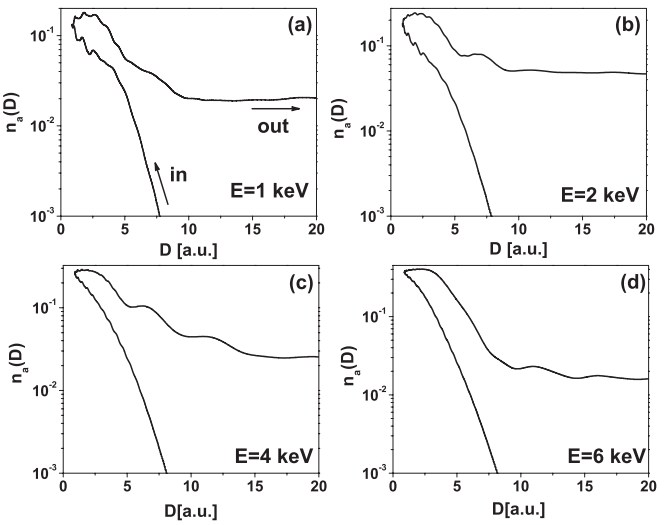

FIG. 11. Transient H^- fractions for grazingly incident hydrogen atoms specularly reflected on a Al(100) surface along the [001] crystal-surface direction with kinetic energies (a) $E = 1$ keV, (b) 2 keV, (c) 3 keV, and (d) 6 keV, corresponding to parallel velocities $v_{||} = 0.19, 0.28, 0.34$, and 0.49 a.u., respectively. The angle of incidence is $\theta = 8^\circ$ in (a), 5.6° in (b), 4.6° in (c), and 3.3° in (d). The incident and outgoing parts of the trajectory are indicated by the arrows in (a).

becomes possible, breaking the approximate circular symmetry of the distributions observed at higher velocities to a discrete symmetry. For instance, electron capture from valence states propagating along the high-symmetry $\bar{\Gamma}\bar{X}$ and $\bar{\Gamma}\bar{M}$ directions of SBZ becomes likely [Figs. 10(c) and 10(d)]. Thus, at low impact velocities (long ion-surface interaction times), electron tunneling is very sensitive to the characteristics of the substrate band structure and the momentum dependence of the charge-transfer couplings.

2. *Grazing incidence*

We now consider projectiles that are grazingly incident at angles relative to the surface between 3.3° and 11.5° and study the dependence of outgoing negative-ion fractions on the surface projected impact velocity $\mathbf{v}_{||}$. The transient hydrogen negative-ion fractions in the specular reflection of hydrogen atoms on the Al(100) surface with collision energies $E = 1$, 2, 4, and 6 keV are shown in Fig. 11, for the same fixed exit-velocity component normal to the surface $v_n = 0.028$. At the lowest collision energy of 1 keV, efficient electron capture from valence states occurs at distances to the surface $D \leqslant 6$ prior to reflection [Fig. 11(a)]. At the point of closest approach the negative-ion fraction reaches $n_a \approx 10\%$. It increases steadily to 15% at $D = 2$ after reflection, as the Doppler shift

$$\varepsilon_n(\mathbf{k}_{||}) \rightarrow \varepsilon_n(\mathbf{k}_{||}) - \mathbf{k}_{||} \cdot \mathbf{v}_{||} \tag{53}$$

brings the AL into resonance with occupied valence states at larger distances to the surface and enables efficient electron capture. The oscillatory structure in the transient distribution that emerges at small distances $D < 2.5$, arises from the lateral corrugation of the surface potential. After reflection, for $D > 3$, continuous electron loss into the conduction band entails a reduction of the anion fraction, which stabilizes near

$n_a = 2\%$ at the freezing distance $D_s = 10$. The anion fraction being an order of magnitude higher than for normally incident projectiles demonstrates that charge transfer is strongly affected by the parallel velocity component $\mathbf{v}_{||}$.

At the higher collision energy of 2 keV, electron capture on the incident part of the trajectory is more efficient [Fig. 11(b)]. This is due to more frequent close encounters of the projectile with Al atoms. After reflection, electron loss into the conduction band is temporary blocked at distances $D \in [5,7]$, where lateral corrugation effects are too weak to affect the time evolution of the projectile charge state ($n_a \approx 8\%$). After entering the weak-coupling region $D > 7$, electron loss to conduction-band states becomes again allowed and reduces the anion fraction before it stabilizes to $n_a \approx 5\%$ at $D_s = 10$.

At relatively high kinetic energies of 4 keV, electron capture from adjacent Al atoms raises the anion fraction to 30% at the point of the closest approach on the trajectory [Fig. 11(c)]. Noticeably, the survival of H^- on the outgoing part of the projectile trajectory is nonexponential in time and exhibits a steplike variation. Suppression of electron loss to conduction-band states occurs after reflection at distances $D \in [5,7]$, where the H^- fraction stabilizes temporary near $n_a = 10\%$. Electron loss is re-enabled at larger distances $D \in [7,10]$ and reduces the anion fraction to $n_a = 4\%$. For $D \in [10,12.5]$, the H^- fraction stabilizes again near $n_a = 4\%$. This is a manifestation of nonadiabatic couplings that are due to the finite interaction-time interval ($\tau = 70$) over which the density of states redistributes between valence and conduction bands. After this delay in the electron tunneling process, secondary electron loss into the conduction band occurs for $D \in [12.5,15.0]$. The anion yield saturates near $D_s = 15$, demonstrating that the freezing distance D_s strongly depends on the parallel velocity $\mathbf{v}_{||}$. We note in passing that a similar steplike decay can occur for interfering and overlapping resonance states [37,38].

At the highest shown collision energy of 6 keV, the oscillatory structure in the transient distributions has almost disappeared, and the promotion of valence electrons contributes to the projectile charge density [Fig. 11(d)]. The hydrogen-anion yield reaches $n_a = 40\%$ at the point of closest approach. Electron loss to conduction-band states is enhanced after reflection, such that H^- survival becomes less likely. The outgoing yield stabilizes to $n_a = 1.5\%$ at $D_s = 15$.

To analyze these results further, the change of the asymptotic TDOS $S(\varepsilon,t \to \infty)$ [cf. Eq. (16)] as a function of the parallel velocity $v_{||}$ is shown in Fig. 12. At a collision energy of 1 keV, the TDOS shown in Fig. 12(a) is centered at conduction-band energies and displays a broad resonance structure. The low-density part of the distribution extends below the Fermi level into the valence band and determines the efficiency of H^- formation. Changing the parallel velocity results in a redistribution of states in the TDOS. When the collision energy is raised to 2 keV [Fig. 12(b)], the spectral weight shifts to the surface ionization threshold. At the same time, the surface density of states increases in the valence band, causing a substantial increase of the hydrogen negative-ion fraction. Further increase of the parallel velocity in Fig. 12(c) continues to increase the spectral weight in the tunneling regime close to the ionization threshold. A new resonance

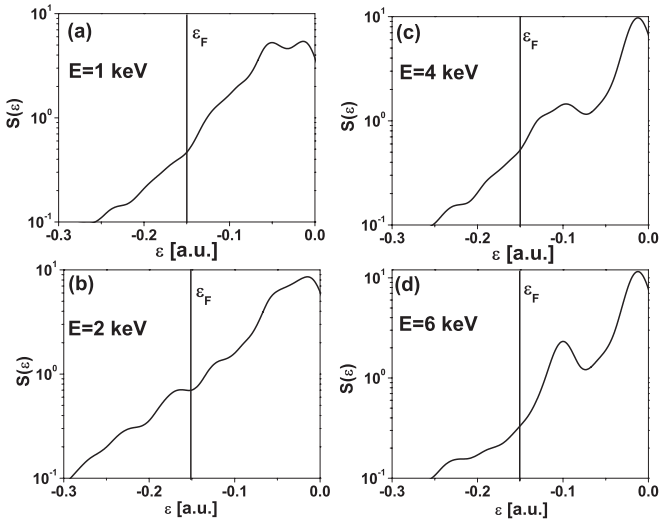

FIG. 12. Asymptotic tunneling density of states $S(\varepsilon,t \to \infty)$ projected onto the hydrogen AL [cf. Eq. (16)]. Results for grazingly incident hydrogen atoms that are specularly reflected on an Al(100) surface along the [001] crystal-surface direction with kinetic energies (a) $E = 1$ keV, (b) 2 keV, (c) 3 keV, and (d) 6 keV, corresponding to parallel velocities $v_{||} = 0.19$, 0.28, 0.34, and 0.49 a.u., respectively. The angle of incidence is $\theta = 8^\circ$ in (a), 5.6° in (b), 4.6° in (c), and 3.3° in (d). The position of the Fermi level is indicated by the vertical solid lines.

structure starts to develop above the Fermi level near $\varepsilon = -0.1$, reducing the contribution of electron capture from the valence band. At larger collision energies of 6 keV [Fig. 12(d)], this resonance state gains amplitude at conduction-band energies. Electron loss thus becomes efficient and anion fractions tend to decrease with the increasing parallel velocity.

The H^- fractions as a function of the parallel velocity are shown in Fig. 13 for the fixed normal exit velocity $v_n = -0.028$. Hydrogen negative-ion formation is unlikely at low parallel speeds $v_{||} \leqslant 0.1$, since the TDOS closely follows the adiabatic PDOS. For increasing parallel velocities $v_{||} > 0.1$, the anion fractions steadily increase. The velocity distribution attains a maximum near $v_{||} = 0.3$ ($E = 2$ keV), when direct

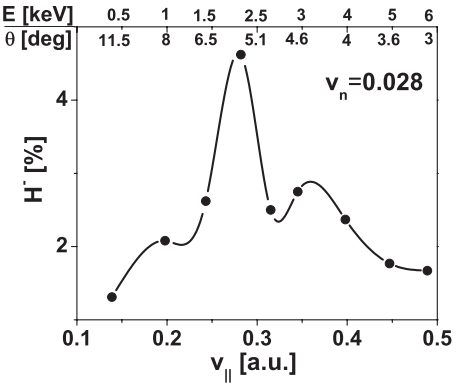

FIG. 13. H^- fractions as a function of the parallel velocity $v_{||}$ for incident H atoms that are specularly reflected on an Al(100) surface along the [001] crystal-surface direction with fixed exit-velocity component normal to the surface $v_n = 0.028$ a.u.. The corresponding collision energies E and the incidence angles θ are indicated along the top horizontal axis.

collision-induced target ionization is energetically allowed via lateral Doppler shift, i.e., for

$$k_{||}v_{||} \geqslant W_{\text{theor}}, \tag{54}$$

where $W_{\text{theor}} = 4$ eV is the work function of the substrate. Near $v_{||} = 0.35$, the distribution attains a second maximum, with much smaller amplitude. The overall decrease of the anion fraction with increasing parallel velocity $v_{||} > 0.35$ is due the redistribution in the density of states. The TDOS shifts toward high energies close to ionization threshold, which enhances electron loss and reduces the efficiency of H^- formation via electron capture from the Fermi sea. Similar effects are found in the measured hydrogen negative-ion yields near Cu(111) and Cu(110) surfaces [3].

3. Directional dependence of charge transfer

The directional dependence of charge transfer near the Al(100) surface is shown in Fig. 14 in terms of the initial-momentum-resolved valence-electron distribution (51). Figure 14 indicates a collision-energy-dependent change in the matching of the electron momenta $\mathbf{k}_{||}$ to the surface-projected projectile velocity $\mathbf{v}_{||}$ for the fixed normal exit velocity $v_n = 0.028$. At the low collision energy of 500 eV in Fig. 14(a), valence electrons have a broad momentum distribution and distribute to favor states pointing in the high-symmetry $\bar{\Gamma}\bar{X}$ and $\bar{\Gamma}\bar{M}$ directions in the SBZ [cf. Fig. 2(a)]. When the collision energy is raised to 2 keV, the momentum distribution narrows, "recoils," and gains amplitude in the direction opposite to $\mathbf{v}_{||}$. Valence electrons are captured predominantly from laterally propagating states pointing in the $\bar{\Gamma}\bar{X}$ direction. Raising the collision energy above the critical energy $E_{\text{crit}} = 2$ keV to

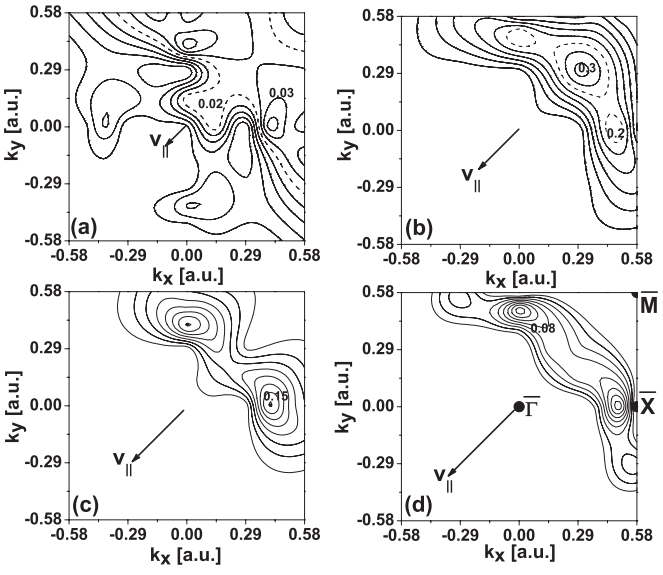

FIG. 14. Initial-state-resolved valence-electron distribution $\sigma(a \leftarrow \mathbf{k}_{||})$ for grazingly incident hydrogen atoms reflected as H^- on an Al(100) surface with kinetic energies (a) $E = 500$ eV, (b) 2 keV, (c) 4 keV, and (d) 6 keV, corresponding to parallel velocities $v_{||} = 0.14$, 0.28, 0.39, and 0.49 a.u., respectively. The angles of incidence are (a) $\theta = 11.5°$, (b) 5.6°, (c) 4°, and (d) 3.3°. The high-symmetry points in the SBZ are indicated in (d). The arrows show the surface-projected collision velocity $\mathbf{v}_{||}$.

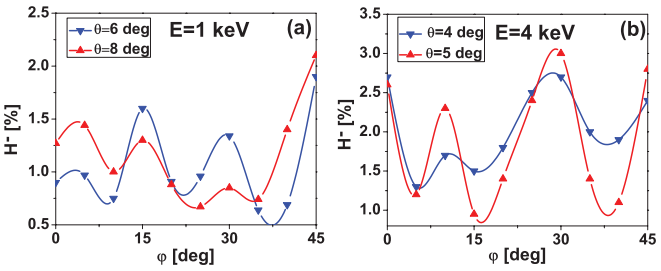

FIG. 15. (Color online) Surface-orientation dependence of the H^- fraction $n_a(E,\theta,\varphi)$ after the reflection of hydrogen atoms on an Al(100) surface. The angle of incidence θ is measured relative to the surface plane. φ is the angle between the surface-projected impact velocity $\mathbf{v}_{||}$ and the [011] crystal-surface direction. (a) Azimuthal variation of the H^- yield at a collision energy of 1 keV for incidence angles $\theta = 6°$ (inverted triangles) and 8° (upward-pointing triangles). (b) Azimuthal variation of the H^- yield at a collision energy of 4 keV and incidence angles $\theta = 4°$ (inverted triangles) and 5° (upward-pointing triangles).

4 and 6 keV [Figs. 14(c) and 14(d)], electrons redistribute to states pointing in the $\bar{\Gamma}\bar{M}$ direction with $\mathbf{k}_{||} \approx (-v_x, 0)$ and to symmetry-equivalent states with $\mathbf{k}_{||} \approx (0, -v_y)$, such that $k_{||} \approx v_{||}$ (momentum matching). At the same time the probability for electron capture has decreased substantially at the increased collision energy. Thus, electron transfer on the Al(100) surface exhibits a directional dependence, which is strongly affected by kinematic shifts and the momentum anisotropy of the charge-transfer couplings.

The directional dependence of electron transfer on the Al(100) surface is analyzed in more detail by scattering projectiles along different crystal-surface directions specified by the angle φ measured relative to the [011] direction for a fixed grazing angle of incidence θ. Figure 15 shows the H^- fractions $n_a(E,\theta,\varphi)$ as functions φ for incidence angles of $\theta = 6°$ and 8° [Fig. 15(a)] and $\theta = 4°$ and 5° [Fig. 15(b)] at collision energies of 1 and 4 keV, respectively. The anion fractions show rapid oscillations, with maxima close to the low Miller index azimuth directions ($\varphi = 0°, 15°, 30°$, and 45°) and minima at high Miller-index directions (less densely packed rows of Al atoms). Though final fractions are small and do not exceed 3%, the anion yield changes by a factor of 3–4 as a function of φ.

4. Comparison with experimental data

In Fig. 16 we compare our theoretical results with the anion yields on Al surfaces measured by Maazouz *et al.* [1] for scattering along the low Miller-index [010] crystal-surface direction for which our calculated anion fractions n_a are maximal (cf. Fig. 15). For comparison, we also computed anion fractions n_a^0 excluding transitions to ionized metal states (by truncating the continuum of substrate energy levels at the vacuum level). At the lower collision energy of 1 keV [Fig. 16(a)], we find that target ionization does not affect the final anion fractions at high normal exit velocities $v_n \geqslant 0.045$. For grazingly incident projectiles with velocities $v_n < 0.045$, the effect of target ionization increases the anion fractions n_a by a factor of 2 relative to n_a^0. At the higher collision energy of 4 keV, the difference between n_a^0 and n_a amounts to

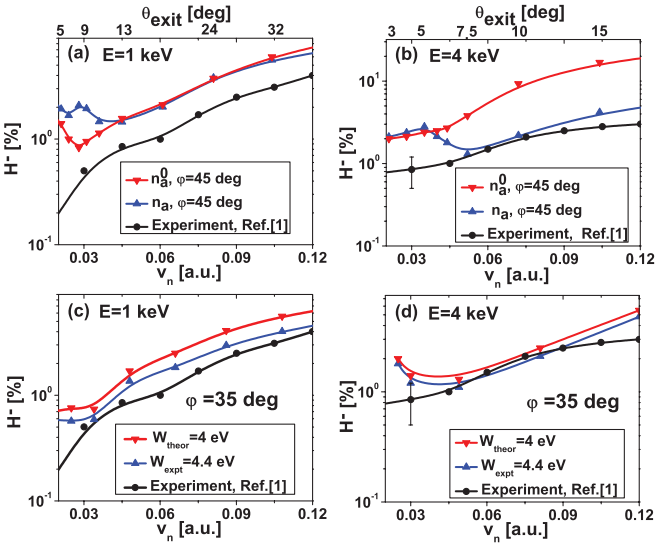

FIG. 16. (Color online) Percentage H^- yields on an Al(100) surface as functions of the exit-velocity component perpendicular to the surface v_n for collision energies of (a), (c) 1 keV and (b), (d) 4 keV in comparison with experimental results of Ref. [1]. The experimental H^- fractions are indicated by the dots (with interpolated solid black lines). φ is the angle between the surface-projected projectile velocity $\mathbf{v}_{||}$ and the [011] crystal-surface direction. (a), (b) Anion yields including (n_a) and excluding (n_a^0) transitions to ionized metal states for $\varphi = 45^\circ$. The anions yields are calculated for the substrate work function $W_{\text{theor}} = 4$ eV. The top horizontal axis gives the exit angle with respect to the surface θ_{exit}. (c), (d) Anion yields n_a for $\varphi = 35^\circ$ calculated for both $W_{\text{theor}} = 4$ eV and the measured work function $W_{\text{expt}} = 4.4$ eV.

about a factor of 6 at the highest exit velocity in Fig. 16(b). The difference between n_a and n_a^0 is negligible for grazingly incident projectiles with $v_n < 0.045$. Thus, we find good semiquantitative agreement with the experiment, at both 1 and 4 keV, only when we include target ionization during the collision. Our calculated anion fractions do not exceed 7% and overestimate the experiment by a factor of 2 at velocities $v_n \geqslant 0.045$, for which reflections from the substrate are primarily due to binary encounter with a substrate ionic core. Quite similarly, the reported experimental anion fractions are near 6–7% at large exit velocities and large exit angles relative to the surface.

The agreement with the experiment for grazing incidence at $v_n < 0.045$ is improved when the projectiles are directed along high Miller index directions (cf. Fig. 15). This is demonstrated for the example $\varphi = 35^\circ$ in Figs. 16(c) and 16(d). The anion fraction at 1 keV reduces to 0.7% for $v_n < 0.045$ and tends to saturate with decrease of the exit velocity, while the 4-keV fraction is slightly below 2% at the smallest exit velocity. Within the experimental error bar indicated for the 4-keV results, our theoretical yield is in overall fair agreement.

We further note that the theoretical anion fraction decreases when the experimental work function ($W_{\text{expt}} = 4.4$ eV [39,40]) of the Al(100) surface is used in computing n_a according to (15), rather than the theoretical work function $W_{\text{theor}} = 4$ eV [Figs. 16(c)–16(d)] we employed so far. The increase of the substrate work function lowers the 1-keV fractions and improves the agreement with the experiment [Fig. 16(c)]. The 4-keV fraction is only weakly affected by the increase of the Al work function [Fig. 16(d)]. Thus, for the collision energies of 1 and 4 keV considered in Refs. [1,2] and employing the measured Al work function, we find good quantitative agreement with the measured anion yields over a wide range of exit velocities components $0.03 \leqslant v_n \leqslant 0.12$ for scattering along high Miller index directions.

IV. CONCLUSION

We calculated the fraction of hydrogen negative ions after the reflection of hydrogen atoms from an Al (100) surface for collision energies between 10 and 6 keV. We found that the charge-transfer dynamics depends sensitively on the projectile impact velocity $\mathbf{v}$, the orientation of the Al crystal surface, and the substrate work function. More specifically, our final negative-ion fractions change nonmonotonically with the projectile velocity, due to the interplay of kinematic-resonance, band-structure, and ion-surface interaction-time effects. For normally incident projectiles, we calculated very small electron-capture probabilities at low collision velocities $v_n \leqslant 0.02$ (long interaction times), consistent with the fixed-ion approximation. For higher impact velocities $0.045 \leqslant v_n \leqslant 0.3$ (shorter interaction times), we found nonadiabatic electron transfer from deep valence-electron levels to enhance H^- formation on the outgoing part of the surface-reflected ion trajectory. Anion formation is unlikely for short interaction times ($v_n > 0.4$), due the small strength of the charge-transfer coupling.

Similarly, we found a nonmonotonic change of the H^- yield by varying the surface-projected projectile-velocity component $v_{||}$. This dependence is tied to the characteristics of the Al band structure and the anisotropy of the (crystal-) momentum-dependent electron-transfer couplings, which give rise to a directional variation of electron transfer. Our calculated outgoing H^- fractions exhibit sensitive polar and azimuthal angular dependencies. They show that H^- formation is favored for projectile incidence along low Miller-index directions and less likely for scattering along high-indexed crystal azimuthal directions. Our calculated hydrogen anion fractions are in good quantitative agreement with the measured H^- yields of Ref. [1].

ACKNOWLEDGMENTS

This work was supported by US NSF Grant No. PHY 1068752 and the Division of Chemical Sciences, Office of Basic Energy Sciences, Office of Energy Research, US DOE.

APPENDIX

The amplitudes $\{S_{ak}\}$ in Eq. (9) are determined from a system of coupled first-order differential equations by including target ionization in terms of continuum-continuum transition amplitudes, $\{S_{lk}\}$,

$$i\frac{dS_{lk}}{dt} = \varepsilon_l S_{lk} + \int dt' \sigma_{la}(t,t') S_{ak}(t') + \sum_{l'} \int dt' \sigma_{ll'}(t,t') S_{l'k}(t') + V_{lk}(t), \quad \text{(A1)}$$

$$i\frac{dS_{ak}}{dt} = \varepsilon_a S_{ak} + \int dt' \sigma_{aa}(t,t') S_{ak}(t') + \sum_l \int dt' \sigma_{al}(t,t') S_{lk}(t') + V_{ak}(t). \quad \text{(A2)}$$

The solutions

$$S_{lk}(t) = \sum_{l'} \int dt' G_{ll'}(t,t') \int dt'' \sigma_{l'a}(t',t'') S_{ak}(t'') + \sum_{l'} \int dt' G_{ll'}(t,t') V_{l'k}(t') \quad \text{(A3)}$$

are expressed in terms of the Green's function $G_{ll'}$ (for propagation in the subspace of the ionized substrate states) that satisfies

$$i\frac{\partial G_{ll'}(t,t')}{\partial t} = \delta(t-t') + \varepsilon_l G_{ll'}(t,t') + \sum_{l''} \int dt'' \sigma_{ll''}(t,t'') G_{l''l'}(t'',t'). \quad \text{(A4)}$$

Inserting the result for $\{S_{lk}\}$ into (A2) and taking advantage of the separability of the couplings $V_{lk} = u_l^* V_k$ in the zero-range model motivates the new definitions for the couplings of the AL to bound metal states in (10) and (11). Using these definitions, we recast the equations of motion into the form of (9), where the inverse "dielectric" kernel,

$$\epsilon^{-1}(t,t') = \delta(t-t') + \int_{t'}^{t} d\tau \sigma_{aa}(t,\tau)\Pi(\tau,t'), \quad \text{(A5)}$$

is defined by (A4) in terms of $G_{ll'}$ and by the coupling parameters γ_l in (13) with

$$\Pi(t,t') = \sum_{l,l'} \gamma_l(t) G_{ll'}(t,t') \gamma_{l'}^*(t'). \quad \text{(A6)}$$

Π satisfies the integral Dyson equation,

$$\Pi(t,t') = \Pi_0(t,t') + \int d\tau \Pi_0(t,\tau) \int d\tau' \sigma_{aa}(\tau,\tau')\Pi(\tau',t'). \quad \text{(A7)}$$

Using (13) and (A7), we find that (12) defines the response kernel ϵ used in the time integration of the equations of motion (9).

[1] M. Maazouz, R. Baragiola, A. Borisov, V. A. Esaulov, S. Lacombe, J. P. Gauyacq, L. Guillemot, and D. Teillet-Billy, Surf. Sci. **364**, 568 (1996).
[2] M. Hosoda, H. Mimura, N. Ohtani, K. Tominaga, K. Fujita, T. Watanabe, H. Inomata, and M. Nakayama, Phys. Rev. B **55**, 13689 (1997).
[3] T. Hecht, H. Winter, A. G. Borisov, J. P. Gauyacq, and A. K. Kazansky, Phys. Rev. Lett. **84**, 2517 (2000).
[4] A. G. Borisov, A. K. Kazansky, and J. P. Gauyacq, Phys. Rev. Lett. **80**, 1996 (1998).
[5] A. G. Borisov, A. K. Kazansky, and J. P. Gauyacq, Phys. Rev. B **59**, 10935 (1999).
[6] P. Kürpick, U. Thumm, and U. Wille, Phys. Rev. A **56**, 543 (1997).
[7] P. Kürpick, U. Thumm, and U. Wille, Phys. Rev. A **57**, 1920 (1998).
[8] P. Kürpick and U. Thumm, Phys. Rev. A **58**, 2174 (1998).
[9] U. Thumm and J. S. Briggs, Nucl. Instrum. Methods Phys. Res., Sect. B **43**, 471 (1989).
[10] L. Guillemot and V. A. Esaulov, Phys. Rev. Lett. **82**, 4552 (1999).
[11] H. Chakraborty, T. Niederhausen, and U. Thumm, Phys. Rev. A **69**, 052901 (2004).
[12] H. Chakraborty, T. Niederhausen, and U. Thumm, Phys. Rev. A **70**, 052903 (2004).
[13] H. Chakraborty, T. Niederhausen, and U. Thumm, Nucl. Instrum. Methods Phys. Res., Sect. B **241**, 43 (2005).
[14] B. Bahrim, B. Makarenko, and J. W. Rabalais, Surf. Sci. **594**, 62 (2005).
[15] A. Schmitz, J. Shaw, H. S. Chakraborty, and U. Thumm, Phys. Rev. A **81**, 042901 (2010).
[16] A. G. Borisov, D. Teillet-Billy, and J. P. Gauyacq, Phys. Rev. Lett. **68**, 2842 (1992).
[17] M. Winter, E. V. Chulkov, and U. Höfer, Phys. Rev. Lett. **107**, 236801 (2011).
[18] G. Fratesi, G. P. Brivio, P. Rinke, and R. W. Godby, Phys. Rev. B **68**, 195404 (2003).
[19] C. Jung, M. Müller, and I. Rotter, Phys. Rev. E **60**, 114 (1999).
[20] U. Fano, Phys. Rev. **124**, 1866 (1961).
[21] P. W. Anderson, Phys. Rev. **124**, 41 (1961).
[22] J. Burgdörfer, E. Kupfer, and H. Gabriel, Phys. Rev. A **35**, 4963 (1987).
[23] R. Brako and D. M. Newns, Rep. Prog. Phys. **52**, 655 (1989).
[24] T. Kirchner, M. Horbatsch, H. J. Lüdde, and R. M. Dreizler, Phys. Rev. A **62**, 042704 (2000).
[25] B. Obreshkov and U. Thumm, Phys. Rev. A **74**, 012901 (2006).
[26] R. Dreizler and E. K. U. Gross, *Density Functional Theory* (Springer, Berlin, 1990).
[27] P. A. M. Dirac, Proc. Cambridge Philos. Soc. **26**, 376 (1930).
[28] E. P. Wigner, Trans. Faraday Soc. **34**, 678 (1938).
[29] N. D. Lang and W. Kohn, Phys. Rev. B **7**, 3541 (1973).
[30] C. Fiolhais, J. P. Perdew, S. Q. Armster, J. M. MacLaren, and M. Brajczewska, Phys. Rev. B **51**, 14001 (1995).
[31] Yu. N. Demkov and V. N. Ostrovsky, *Zero-Range Potentials and their Application in Atomic Physics* (Plenum, New York, 1988).
[32] P. M. Echenique, R. H. Ritchie, N. Barberán, and J. Inkson, Phys. Rev. B **23**, 6486 (1981).
[33] P. J. Feibelman, Prog. Surf. Sci. **12**, 287 (1982).
[34] B. Obreshkov and U. Thumm, Phys. Rev. A **83**, 062902 (2011).
[35] A. G. Borisov, D. Teillet-Billy, and J. P. Gauyacq, Surf. Sci. **278**, 99-110 (1992).
[36] I. Rotter, E. Persson, K. Pichugin, and P. Seba, Phys. Rev. E **62**, 450 (2000).
[37] E. Frishman and M. Shapiro, Phys. Rev. Lett. **87**, 253001 (2001).
[38] C. Makochekanwa, O. Sueoka, and M. Kimura, Phys. Rev. A **68**, 032707 (2003).
[39] J. K. Grepstad, P. O. Garland, and B. J. Slagsvold, Surf. Sci. **57**, 348 (1976).
[40] H. B. Michaelson, J. Appl. Phys. **48**, 4729 (1977).